D. Gallart, M. Mantsinen, C. Challis, D. Frigione, J. Graves, E. Belonohy, F. Casson, A. Czarnecka, J. Eriksson, J. Garcia, M. Goniche, C. Hellesen, J. Hobirk, P. Jacquet, E. Joffrin, N. Krawczyk, D. King, M. Lennholm, E. Lerche, E. Pawelec, et al

Modelling of JET hybrid plasmas with emphasis on performance of combined ICRF and NBI heating

Modelling of JET hybrid plasmas with emphasis on performance of combined ICRF and NBI heating

D. Gallart, M. Mantsinen, C. Challis, D. Frigione, J. Graves, E. Belonohy, F. Casson, A. Czarnecka, J. Eriksson, J. Garcia, M. Goniche, C. Hellesen, J. Hobirk, P. Jacquet, E. Joffrin, N. Krawczyk, D. King, M. Lennholm, E. Lerche, E. Pawelec, et al

Modelling of JET hybrid plasmas with emphasis on performance of combined ICRF and NBI heating

D. Gallart[1], M.J. Mantsinen[1,2], C. Challis[3], D. Frigione[4], J. Graves[5], E. Belonohy[6], F. Casson[3], A. Czarnecka[7], J. Eriksson[8], J. Garcia[9], M. Goniche[9], C. Hellesen[8], J. Hobirk[6], P. Jaquet[3], E. Joffrin[9], N. Krawczyk[7], D. King[3], M. Lennholm[10], E. Lerche[11], E. Pawelec[12], X. Sáez[1], M. Sertoli[6], G. Sips[6], E. Solano[13], M. Tsalas[14], P. Vallejos[8], M. Valisa[15] and JET Contributors*

[1]Barcelona Supercomputing Center (BSC)
[2]ICREA, Barcelona, Spain
[3]CCFE, Culham Science Centre, Abingdon, Oxon, OX14 3DB, UK
[4]Associazione EURATOM-ENEA, C.R.E. Frascati, Italy
[5]Centre de Recherches en Physique des Plasmas, EPFL, 1015, Lausanne, Switzerland
[6]Max-Planck-Institut fur Plasmaphysik, Garching, Germany
[7]Institute of Plasma Physics and Laser Microfusion, Association EURATOM/IPPLM, Poland
[8]Uppsala University, Euratom/VR Fusion Assoc., Uppsala, Sweden
[9]CEA, Centre d'Etudes Nucleaires de Cadarache, France
[10]European Comission, B-1049 Brussels, Belgium
[11]Laboratory for Plasma Physics, LPP-ERM/KMS, Brussels, Belgium
[12]Institute of Physics, Opole University, ul. Oleska 48, Opole 45-052, Poland
[13]Association EURATOM-CIEMAT para Fusion, CIEMAT, Madrid, Spain
[14]FOM institute DIFFER, Association EURATOM-FOM, PO Box 120, Nieuwegein, Netherlands
[15]Consorzio RFX, Associazione Euratom-ENEA sulla Fusione, Padova 35137, Italy

E-mail: `daniel.gallart@bsc.es`

Abstract. During the 2015-2016 JET campaigns many efforts have been devoted to the exploration of high-performance plasma scenarios envisaged for DT operation in JET. In this paper we review various key recent hybrid discharges and model the combined ICRF+NBI heating. These deuterium discharges with deuterium beams had the ICRF antenna frequency tuned to match the cyclotron frequency of minority H at the centre of the tokamak coinciding with the second harmonic cyclotron resonance of D. The modelling takes into account the synergy between ICRF and NBI heating through the second harmonic cyclotron resonance of D beam ions which allows us to assess its impact on the neutron rate R_{NT}. For discharges carried out with a fixed ICRF antenna frequency and different toroidal magnetic field to vary the resonance position, we evaluate the influence of the resonance position on the heating performance and central impurity control. The H concentration was varied in different discharges in order to test its role in the heating performance. It was found that discharges with a

---

* See the author list of "X. Litaudon et al 2017 Nucl. Fusion 57 102001"

resonance beyond ~ 0.15 m from the magnetic axis R_0 suffered from MHD activity and impurity accumulation in these plasma conditions. According to our modelling, the ICRF enhancement of R_{NT} increases with the ICRF power absorbed by deuterons as the H concentration decreases. We find that in the recent hybrid discharges this ICRF enhancement varied due to a variation of H concentration and was in the range of 10-25%. The modelling of a recent record high-performance hybrid discharge shows that ICRF fusion yield enhancement of $\sim$30% and $\sim$15% can be achieved in the ramp-up phase and during the main heating phase, respectively. We extrapolate the results to DT and find that the best performing hybrid discharges correspond to an equivalent fusion power of $\sim$7.0 MW in DT. Finally, an optimization analysis of the bulk ion heating for the DT scenario reveals around 15-20% larger bulk ion heating for the ^{3}He minority scenario as compared to the H minority scenario.

1. Introduction

Among the envisaged auxiliary heating systems for ITER, ion cyclotron resonance frequency (ICRF) heating has proved to be an efficient mechanism to bring plasmas at high temperatures in present-day tokamaks. ICRF heating demonstrated its capabilities for heating of reactor-like plasmas in DT scenarios relevant for ITER in TFTR [1, 2] and during the 1997 DT campaign in JET [3–5]. Several studies have been conducted for the initial non-activated phase of ITER, where the reference ICRF heating scenarios rely on minority species such as 3-helium (^{3}He) or deuterium (D) in hydrogen (H) majority plasmas [6, 7]. Moreover, ICRF has many applications beyond heating due to its interaction with the plasma [8], bringing the flexibility for a wide range of different experiments such as the mimicking of fusion-born alphas [9] or the production of super energetic particles with the novel three-ion scheme [10]. ICRF heating also plays an important role in achieving high-performance discharges via optimization of bulk ion heating [11–13], fusion enhancement [14, 15] and core impurity control [16–18].

During the 2015-2016 JET campaigns with the ITER-like-wall (ILW) many efforts have been devoted to the exploration of high-performance plasma scenarios envisaged for ITER operation [19]. The inductive (baseline) scenario [20] and the hybrid scenario [21] have achieved major improvements during these campaigns surpassing the previous ILW fusion record of $2.3 \cdot 10^{16}$ neutrons/s, thus showing good progress towards demonstrating the fusion rate goal for DT (the objective for DT-ready plasma is $6 \cdot 10^{16}$ s^{-1} for 5 s [22]). The hybrid scenario reached with 33 MW of combined ICRF and NBI power a record neutron rate R_{NT} of $2.9 \cdot 10^{16}$ s^{-1}. The hybrid scenario is an advanced regime expected to be applied in ITER. It is characterized by a low plasma current I_p which allows operation at a high normalised beta $\beta_N = \langle \beta \rangle aB_T/I_p$ and a q profile ($q(0) \geq 1$) that prevents sawtoothing m=1, n=1 (1/1) MHD activity in the core from triggering large NTMs [21]. In preparation for the next DT campaign at JET with the ILW planned for 2020, the analysis of this scenario's heating performance is of great relevance as it gives insight on the strategy to follow in order to obtain the objective of a fusion reaction rate of $6 \cdot 10^{16}$ s^{-1} for 5 s [22].

This paper studies the heating performance of the recent hybrid discharges where we model and assess the performance of ICRF+NBI heating and the fusion enhancement through ICRF heating. The aim is to predict the fusion performance of the best discharges with a DT plasma giving an estimation of their associated fusion power. Hence, this paper provides the reader with a description of the ICRF and NBI heating modelling and the impact of these heating mechanisms on the fusion yield of the recent hybrid discharges at JET. In order to do so, we evaluate the performance of H minority heating in the presence of D beam ions using the ICRF modelling code PION [23] coupled [11] to the beam deposition code PENCIL [24]. Our modelling also takes into account the synergy between ICRF and NBI heating through the second harmonic cyclotron resonance of D beam ions, which allows us to assess its impact on the fusion performance. The hybrid discharges analysed in this paper were composed of minority

H and a majority of D together with a low concentration of certain impurities such as beryllium (Be) or carbon (C). The antenna was tuned to the H fundamental resonance which coincides with the 2nd D harmonic resonance ($\omega = \omega_H = 2\omega_D$) and in most cases it was a central resonance, $s \approx 0.05 - 0.1$ and ranging to $s \approx 0.2$ for discharges with an off-axis resonance, where s is the square-root of the normalised poloidal flux. The analysis shows that for optimal plasma conditions with high plasma temperature, low H concentration and the presence of D beams, most of the ICRF power is coupled to D which has beneficial effects to the fusion yield.

Given the relevance and interest shown in the forthcoming 2018-2020 JET campaigns in the performance of different ICRF heating schemes in order to boost heating and fusion yield, we have prepared, in addition to the modelling of the experimental scenarios with H minority, a comparison in section 8.2 of ^{3}He and H minority in a DT plasma where we assess the bulk ion heating efficiency under a scan of relevant plasma parameters. For these cases, the antenna frequency was tuned to the ^{3}He fundamental resonance which coincides with the 2nd tritium (T) harmonic resonance ($\omega = \omega_{^3He} = 2\omega_T$). Central heating with a resonance at $s = 0.01 - 0.05$ was considered.

We model a number of key discharges that were designed in order to evaluate key ICRF aspects. Therefore, in order to assess the best strategy to follow in terms of ICRF heating we have organised our modelling analysis in the following way: (1) the avoidance of impurity accumulation with ICRF waves and its dependence on the ICRF resonance position, (2) the impact of H concentration on the ICRF damping mechanisms, i.e, the fundamental H resonance, the 2nd D harmonic resonance and the direct electron damping, (3) the analysis of combined ICRF and NBI in high-performance hybrid discharges and their associated ICRF fusion performance enhancement. And (4) the prediction for a record discharge to a 50:50 DT fuel mixture including the analysis of the optimal conditions to maximize bulk ion heating.

In order to validate our modelling for JET discharges we can not rely on direct measurements of ICRF local power density absorption as they are not available. However, we have calculated ICRF-related quantities such as the neutron production and the enhancement by ICRF of the fusion yield and then compared with the experimental data to show that our modelling is consistent with the experiments.

Including this introduction our paper is organised in 8 sections comprising the theoretical background of the analysis (section 2), the numerical methods used (section 3), the general parameters of the hybrid scenario studied (section 4), the discussion of the modelling results (sections 5-8) and finally the conclusions (section 9). This paper is the continuation and the extension of a series of papers devoted to the ICRF modelling of hybrid discharges Refs. [25–28].

2. Theoretical Background

Here we discuss the ICRF physics involved in the analysis of the modelling results, especially those that have direct impact on the fusion performance: ICRF power

partition, power partitioning between ions and electrons and mechanisms to influence impurity transport by ICRF waves.

2.1. Power partition

Three damping mechanisms compete in the discharges studied in this paper, i.e., the ion cyclotron resonance of H and D through fundamental hydrogen resonance ($\omega = \omega_H$) and 2nd D harmonic resonance ($\omega = 2\omega_D$), direct electron damping via electron Landau Damping (ELD) and transit time magnetic pumping (TTMP). Direct electron damping may play an important role in those discharges with high electron densities and temperatures and when the resonance position is located at the high-field side (HFS). For the plasma temperatures and densities of this hybrid high-performing discharges direct electron damping typically damps 10-20% of the wave energy as will be shown in sections 6 and 7. As a reference, a theoretical expression for direct electron damping in H minority and bulk D plasmas is given as in [29]

$$2\eta \simeq L\frac{\pi^{1/2}}{2}\frac{\omega}{\Omega_D}\frac{\omega_{pD}}{c}\beta_e\zeta_e e^{-\zeta_e^2}, \tag{1}$$

where 2η is the optical depth where the wave arriving at the minority cyclotron resonance is absorbed by a single-pass absorption factor, $A = 1 - e^{-2\eta}$, $L \simeq 2a/3$ is an effective radial absorption length assuming $\zeta_e \simeq 1$, $\zeta_e = \omega/k_\parallel v_{te}$, $v_{te} = (2T_e/m_e)^{1/2}$, β_e is the bulk electron beta, Ω_D is the fundamental D cyclotron angular frequency and ω_{PD} is the deuterium angular plasma frequency. Direct electron damping is typically maximum on axis where T_e peaks.

Fundamental H damping is particularly important during the ramp-up, when the plasma is still cold and in the absence of D beams. The 2nd D harmonic depends strongly on the velocity distribution of D, becoming more relevant as an energetic D tail develops, i.e. with the D beams. The local power partition between D harmonic and H fundamental can be approximated by calculating the second moment of the Fokker-Planck RF operator and including FLR effects to the lowest order in the Taylor expansion of the diffusion coefficient for the 2nd D harmonic as done in [11, 23]:

$$\frac{p_2}{p_1} = c_{21}\frac{k_\perp^2 w_2}{n_1 m_1 \omega_{c2}^2}. \tag{2}$$

Here, the subscripts 1 and 2 refer to the resonant species with a fundamental and a 2nd harmonic resonance, respectively, p_1 and p_2 are the local power densities absorbed by H and D, respectively, $k_\perp$ is the perpendicular wavenumber, w_2 is the energy density of deuterium, n_1 and m_1 are the hydrogen density and mass, respectively, ω_{c2} is the cyclotron frequency of D and c_{21} is a constant. The analysis of JET high-performance hybrid discharges with PION shows that $c_{21} \approx 0.2-0.3$. This parameter is not universal as it may vary for different scenarios. The value is calculated as an average for different power absorption ratios given by PION for discharges presented in this study.

In the experiments we lowered the H concentration so the D power absorption increased, as can be seen in (2). Another important factor is the D beam injection which

increases substantially the D energy density and consequently the D power absorption. These two joint effects contributed to achieving the highest fusion yield that has been reached in the hybrid discharges.

For the DT prediction we have considered two ICRF scenarios, ^{3}He minority and H minority. Strong ion cyclotron damping performance by ^{3}He minority is predicted by PION. ^{3}He absorbs most of the wave energy during all the stages of the discharge, in contrast with the H minority damping performance which typically becomes weaker as D beams are injected. For this scenario the equation (2) is still valid, taking into account that subscripts 1 and 2 refer to ^{3}He and T, respectively. The computed value of constant c_{21} based on PION results is $c_{21} \approx 0.01 - 0.02$.

The 3rd harmonic resonance must be taken into account in the DT prediction with D and T beams when the minority species considered is H. For H minority in DT plasma, the damping performance from resonant H and D ions is similar to that from a pure D plasma. In fact, the 3rd T harmonic resonance does not play a relevant role as it absorbs a small fraction of the wave energy, which is negligible compared to that absorbed by H or D. In order to understand this behavior, we have obtained an equation that describes the local power partition for the 3rd harmonic using the same procedure to compute (2). The local power partition between the 3rd harmonic, fundamental and 2nd harmonic resonant ions scales as,

$$\frac{p_3}{p_1} = c_{31} \frac{m_3 k_\perp^4}{m_1 n_1 \omega_{c3}^4} \int v_3^4 f_3 dv, \quad \frac{p_3}{p_2} = c_{32} \frac{m_3 k_\perp^2 \omega_{c2}^2}{\omega_{c3}^4 w_2} \int v_3^4 f_3 dv. \tag{3}$$

The main difference from (2) comes from the presence of the 4th moment of the distribution function which needs to be computed numerically and the different exponents in the wave number and the cyclotron frequency. However, by assessing the order of magnitude of the terms $k_\perp^2 w_2 / \omega_{c2}^2$ and $k_\perp^4 m_3 \int v_3^4 f_3 dv / \omega_{c3}^4$ for (2) and (3), respectively, for typical values of the scenarios studied we find that there are approximately two orders of magnitude of difference between them, being higher the term in (2). This theoretical approximation explains the weak damping strength observed for the 3rd T harmonic resonance in the simulations performed with PION.

2.2. Bulk ion heating

Major bulk ion heating is necessary to increase the number of thermal fusion reactions. In order to obtain major bulk ion heating the fast ions average energy should not surpass a threshold energy, the so called critical energy. In the process of thermalisation, energetic ions will slow-down by colliding with background ions and electrons, this effect increases the thermal ion and electron temperature, respectively. The energy threshold at which thermal ions and electrons are equally heated is the critical energy [36],

$$E_{crit} = 14.8 A T_e \left[\sum_j \frac{n_j Z_j^2}{n_e A_j} \right]^{\frac{2}{3}}. \tag{4}$$

Here A is the atomic mass of the resonant ion species, T_e is the electron temperature, n_j and n_e are the densities of the j-ith ion species and electrons, respectively, Z_j and A_j are the atomic number and atomic mass of the j-ith ion species, respectively.

The velocity distribution of the resonant ions plays a crucial role in the way the collisional power is transferred. The average fast ion energy must be kept below the critical energy for dominant bulk ion heating. An energetic ion of energy E transfers its energy following $\dot{W}_i/\dot{W}_e = (E_{crit}/E)^{3/2}$ where $\dot{W}_i$ and $\dot{W}_e$ are the rate of energy transfer to thermal ions and electrons, respectively, while E is the energy of the non-thermal ion [36]. This is the instantaneous ratio of energy transfer from an ion to thermal ions and electrons, for a complete slowing-down one needs to integrate over all the energy states of the ion until thermalisation is reached. Here, we show the ratio of the total energy given up by a single ion of energy E to thermal ions after a complete thermalisation as done by Stix in [36] and as an extension to this work we have integrated this ratio over a gaussian centered at the average ion temperature T_i and a Maxwellian for D and H, respectively, which gives an approximation of the energy transferred from fast ions to thermal ions in a simplified case. However, ICRF heating through 2$^{\text{nd}}$ D harmonic resonance drives a strong tail in the D velocity distribution function which is non-Maxwellian and, therefore, figure 1 must be understood as a rough estimation. It has been computed as $\int_0^E G(E)f(E)dE$, where $G(E)$ is the average fraction of the energy transferred from fast ions to thermal ions as defined in [36] and $f(E)$ is a maxwellian distribution for fast ions (figure 1). From the simplified calculation shown in figure 1b)
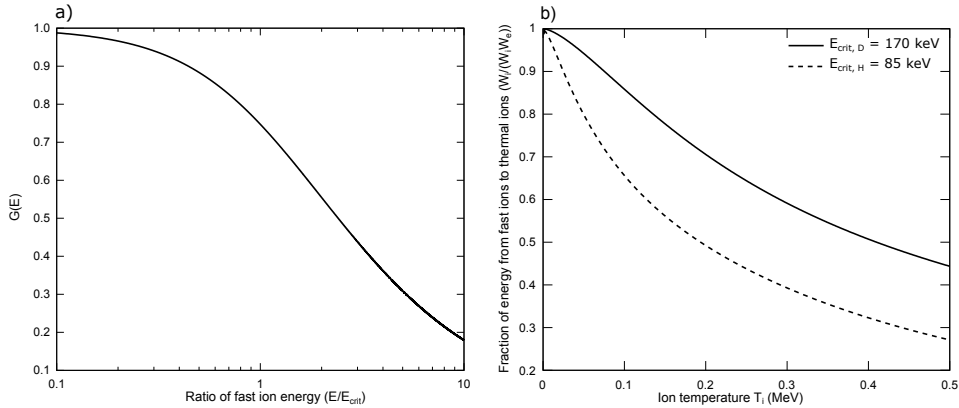
Figure 1: *a) Ratio of energy $G(E)$ given up by a fast ion to thermal ions over a complete thermalisation as in [36], b) $G(E)$ averaged over a gaussian and a maxwellian for different thermodynamic ion temperatures T_i and fixed critical energies for D and H, respectively, $E_{crit,D} = 170$ and $E_{crit,H} = 85$ keV.*

one expects to have dominant bulk ion heating from fast H ions for the discharges considered in this paper. This is not the case during the ramp-up where resonant H ions typically reach an average energy in the range of 500 keV and as will be shown, collisions with electrons are dominant. The average fast ion energy is calculated using the fast ion density energy content and the fast ion density $\langle E_f \rangle = \frac{w_f}{n_f}$ as predicted by

PION where fast ions are computed following the explanation in section 3. Taking into account that D beams are injected at an energy around 110 keV dominant bulk ion heating is expected (figure 1 b)), the addition of ICRF heating can bring a fraction of D ions to energy levels closer or even above the D critical energy. This high energy tail in the D distribution function will lead to different behaviour for DD and DT plasmas in terms of neutron rate production due to differences in the fusion cross section as will be shown in sections 7 and 8.

2.3. On mechanisms to influence W accumulation with ICRF waves

Tungsten (W) in the divertor, Be limiters and exposed inconnel in main chamber are currently the plasma wall facing components of the installed ILW at JET. Tungsten possesses a high temperature tolerance and low erosion rate which make it a strong candidate for the future ITER reactor. However, dilution by any high-Z impurities need to be controled and minimised below a concentration of 10^{-4} in a fusion plasma reactor in order to achieve high-performance discharges.

When poloidal asymmetries are not considered and following the discussion in [17, 30] W flux can be described as:

$$\Gamma_W \sim n_i T_i \nu_{iW} Z_W \left(\frac{R}{L_{n_i}} - 0.5 \frac{R}{L_{T_i}} \right). \tag{5}$$

Here, n_i and T_i are the ion density and temperature, respectively, $\nu_{iW} \sim T_i^{-3/2}$ is the background ion-tungsten collision frequency, R is the major radius and L_{n_i} and L_{T_i} are the inverse of the logarithmic gradient of ion density and temperature, respectively. For ion temperature gradient terms larger than the ion density gradient term, central W accumulation is avoided as the flux convection becomes outward.

Recent studies [17,18,30,34] have proved ICRF heating as an efficient mechanism to avoid central impurity accumulation, mainly through avoidance of poloidal asymmetries and enhancement of temperature screening. In the presence of ICRF heating, temperature screening in (5) is effectively increased by the fast minority temperature screening $\sim n_f T_f^{-1/2} R/L_{T_f}$. Furthermore, fast minority ions tend to become trapped in banana orbits that are localised at the low-field side (LFS) and create a poloidal varying potential that push W to the high-field side (HFS), effectively reducing the poloidal asymmetries as a result of W accumulation at the LFS by plasma rotation. Poloidal asymmetries have been identified to enhance neoclassical transport and to be the main mechanism for central tungsten accumulation [30, 33].

In this paper the analysis has been restricted to hybrid discharges of the campaign with different ICRF resonance positions. Two discharges suffered central impurity accumulation which was accompanied by MHD activity. MHD activity has been resported as the cause of triggering impurity accumulation in hybrid discharges in Ref. [35]. Here, an analysis of the differences of ICRF heating profiles for a scan in the resonance position is performed and temperature screening factors associated with fast

minority ions are calculated taking into account orbit width effects. However, modelling of W transport has not been carried out as it is out of the scope of the present paper.

3. Numerical methods

The hybrid discharges simulated in this paper have two competing ion damping mechanisms, the fundamental H resonance and the 2nd harmonic D resonance ($\omega \approx \omega_H = 2\omega_D$). An accurate description of the velocity distribution of both resonant species is necessary, particularly for higher harmonics $n \geq 2$, where the absorption strength is weak at low perpendicular velocities but increases with higher temperatures until a maximum is reached, typically in the MeV range [37]. For this reason, taking into account the D beams in the velocity distribution function to solve the wave absorption becomes crucial in this scenario. In order to do so, we use the ICRF code PION [23] which solves the power absorption and the velocity distribution function in a self-consistent way using simplified models [38]. The input data necessary to run the PION code is obtained from the JET experimental database, which provides the necessary information to simulate each discharge. All the input from the JET-database is time evolving, such as the equilibrium, antenna wave frequency, minority concentration and plasma parameters. Therefore, PION provides calculations that evolve in time according to the plasma discharge evolution. Data read by PION is stored for different time points and normalized squared root poloidal flux surfaces of a single discharge, therefore, simulations show the evolution in time of absorption profiles and distribution of velocities of resonant ions for the discharge.

At the beginning of a calculation input data are read into PION and the resonating species are assumed to be Maxwellian. A power deposition is then produced and the output is used in the Fokker-Planck module, which advances the distribution function(s) a time step Δt, typically $\Delta t \sim 0.01s$ for discharges analysed here. At the beginning of the next time step, after having read the new input data, output from the Fokker Planck calculation is then used in the ICRF power deposition module and a new power deposition is produced. The distribution functions(s) are then advanced another time step Δt and the process is repeated until the end of the calculation. The power deposition is calculated with the flux surface integrated Poynting flux which is described with the averaged squared parallel velocity of the resonating ions and the single pass absorption coefficient along the cyclotron resonance [23, 39]. The single pass absorption coefficient is calculated as the sum of the absorption coefficients for the resonant ion species. Very small absorption from impurities (carbon, beryllium, helium) is predicted by PION for the discharges analysed here (table 1). To take into account direct electron damping, the flux surface integrated Poynting flux is separated into volume integrated electron and ion absorption as described in [38].

The velocity distribution function is calculated for resonant ion species with a time dependent one dimensional Fokker-Planck equation for the pitch angle averaged

distribution function, $F(v)$,

$$\frac{\partial F}{\partial t} = C(F) + Q(F) + S + L.$$

Here $C(F)$ is the collisional operator, $Q(F)$ is the RF operator, S is a source term included in the distribution function to take into account the source from NBI beams [11] and L is a loss term. The Coulomb diffusion coefficients are calculated for ions colliding with all plasma ions species and electrons that are assumed Maxwellian [23]. PION takes into account finite orbit width effects by averaging the collision coefficients in $C(F)$ over fast ion orbits with finite width and assuming them to be trapped with turning points close to the point where the wave frequency and the cyclotron frequency or its multiples coincide $\omega = n\omega_c$ [3]. Those particles that belong to the non-Maxwellian part of the distribution function $F(v)$ are considered fast particles by PION. The resulting collisional power to bulk ions and electrons is corrected for self-collisions by subtracting the contribution arising from the Maxwellian part of $F(v)$. First orbit losses are included by considering which fast ions are on unconfined orbits. In discharges studied here, there are no first orbit losses according to PION. The averaged square parallel velocity needed for the ICRF power deposition calculation is obtained with the effective pitch angle and integrating over the velocity distribution as described in [38].

For the discharges studied only the D distribution function contains the source term as only D beams were used. For the DT prediction, T beams are included. The beam source terms are calculated using the beam code PENCIL [24]. PENCIL takes into account the injector PINI's that were used (1-16 in these experiments) and the beam molecular fraction (1/1, 1/2 and 1/3). Table 1 shows the average NBI energies and power fractions used. These source terms are then included in the Fokker-Planck distribution function of the PION code for each time point and flux surface [11]. For a given flux surface and injection energy, the NBI source is assumed to be Gaussian in velocity for numerical reasons, with the peak centred at the injection energy corrected for bulk plasma rotation effects, and with a half width typically corresponding to 10-20% of the thermal velocity. The PION code does not calculate the radial transport (except for the effects due to finite orbit widths), hence, in order to keep the consistence between the measured plasma and specially the resonating ion densities with the simulated ones, an ad-hoc procedure is implemented. As described in [11], a portion of a Maxwellian is added when the difference between the densities at the end and at the beginning of the time step for a flux surface is less than the increase in the number of ions due to NBI. Conversely, particle losses are introduced if the beam source terms add more particles than is consistent with the measured particle density on that flux surface. The loss term removes the required number of particles from the thermal background. In the discharges studied here, with a relatively smooth evolution of the density in time, the time step of simulations was chosen so that these losses stayed below 25% of the total number of particles. If this would not have been possible, we would have included an additional loss term implemented in PION that removes the excess particles from the whole distribution function. These source and loss terms are required in the model

in order to simulate the time dependent problem without solving a radial transport equation.

4. General parameters of the hybrid scenario studied

A summary of the main parameters for the studied discharges is shown in table 1. The

Table 1: JET main parameters for studied hybrid scenario discharges. PINI's data is given as for the reference hybrid high-performance discharge 92398.

Parameter	
Major radius R_0 (m)	2.96
Minor radius a (m)	1.25-2.10
Toroidal magnetic field B (T)	2.8
Plasma current Ip (MA)	2.2
Normalised Beta β_N	1.9-2.7
NBI Power $P_{\mathrm{NBI}}(MW)$	20-26
ICRF Power $P_{\mathrm{ICRF}}(MW)$	4-5
Central ion temperature T_{i0} (keV)	8-12
Central electron temperature T_{e0} (keV)	6-8.5
Electron density n_e ($10^{19}\mathrm{m}^{-3}$)	6-7.5
Power absorbed by impurities P_{imp} (MW)	0.01-0.03
Octant 8 PINI (1-8) energy (keV)	98-109
Octant 8 PINI (1-8) power fractions	0.53, 0.33, 0.14
Octant 4 PINI (9-16) energy (keV)	108-109
Octant 4 PINI (9-16) power fractions	0.53, 0.33, 0.14

hybrid discharges presented in the following sections have the same plasma composition, i.e. a small concentration in the range of 1-4% of H in a D plasma. ICRF and NBI heating were present in all discharges and minority heating of H and 2$^{\mathrm{nd}}$ D harmonic heating was the ICRF scheme used. All discharges are explained in each section and are focused on investigating certain key ICRF heating aspects that have an impact on the fusion neutron rate.

5. Effect of resonance position on ICRF heating and impurity control

This first analysis was necessary as to know the limits for off-axis heating and proceed with the rest of the discharges. The resonance position has an impact on the heating profile and also on the impurity accumulation. The analysis of impurity accumulation is complex as many mechanisms are involved in the transport of high-Z impurities. One of such mechanisms is the temperature screening provided by fast ions generated through ICRF heating. Here, the impurity screening associated to H minority and the ICRF

heating profiles are computed using PION for discharges where resonance position was varied.
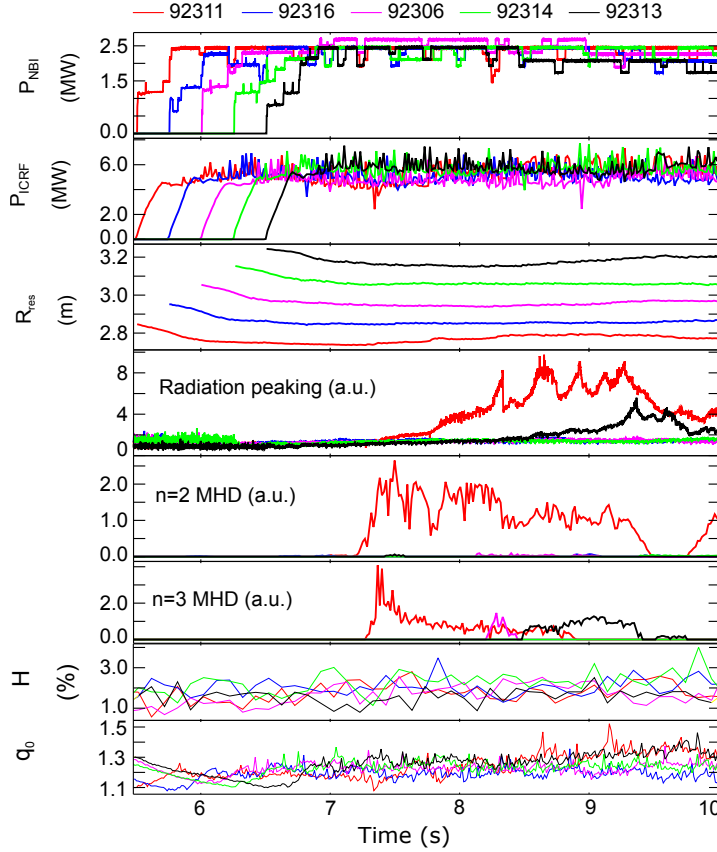
Figure 2: *Overview of five hybrid discharges with combined NBI+ICRF heating at different toroidal magnetic fields to vary the ICRF resonance location: 2.6, 2.7, 2.8, 2.9 and 3.0 T in discharge 92311, 92316, 92306, 92314 and 92313, respectively. The start time of external heating was modified to match the central safety factor at the heating onset.*

The ICRF resonance position was varied in a total of five hybrid discharges in order to assess its impact on the ICRF impurity control. As $R_{res} \propto B_T$, the magnetic field B_T was modified accordingly so as to place the ICRF resonance at different major radii ranging from $R_{res} = 2.75$ m (high-field-side) to $R_{res} = 3.2$ m (low-field-side) while the magnetic axis was located at around $R_0 = 3.0$. There are only a limited sets of antenna frequencies available at JET, therefore in order to scan the resonance position the toroidal magnetic field is varied for a given antenna frequency. Notice that all evolving input parameters such as magnetic field or antenna frequency are taken into account in PION as explained in section 3. A total of 30 MW of combined external heating power was used [25], consisting of 25 MW of NBI and 5 MW of ICRF at a frequency of 42 MHz. An overview of these discharges is shown in figure 2. In order to keep a similar central safety factor among these discharges, the starting time of the external power heating, i.e. ICRF and NBI heating, was delayed 0.25 s for each B_T

change of 0.1 T. Figure 2 shows that those discharges with a resonance $|R_{res} - R_0| > 15$ cm suffered from MHD activity and impurity accumulation in these plasma conditions. The MHD modes (m/n) that were present in the HFS discharge 92311 were 3/2 and 4/3 and assuming the EFIT safety factor profile they were located at s = 0.28 and s = 0.03, respectively. For the LFS discharge 92313 the modes were 5/3 and 4/3 located at s = 0.34 and s = 0.03, respectively. We have selected three discharges as shown in table 2 for detailed analysis. Two discharges that had radiation peaking (92311 and 92313) and a central discharge that did not show radiation peaking, we selected 92314, however, 92306 is very similar too.We refer to them from now on by their ICRF resonance position: HFS, central and LFS.

Table 2: ICRF resonance position for discharges 92311, 92313 and 92314.

	92311	92314	92313
ICRF resonance pos.	HFS	Central	LFS
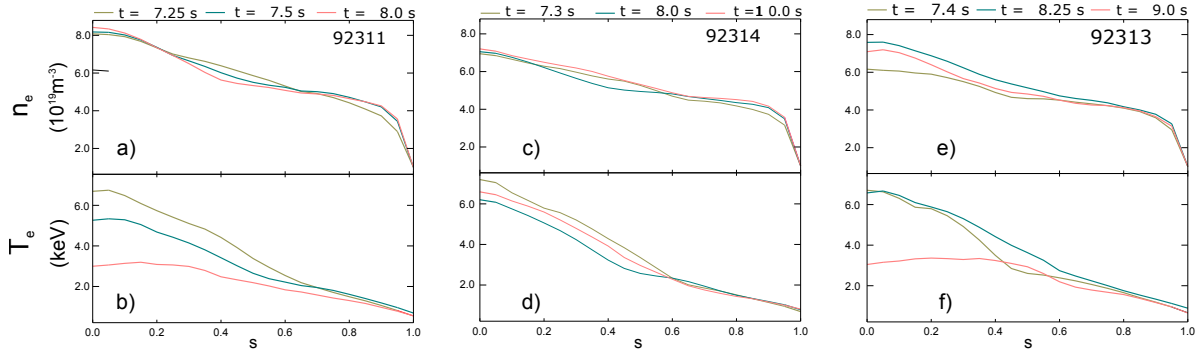
Figure 3: *Electron density and temperature as measured by the LIDR, for HFS discharge 92311 (a) and b)), central discharge 92314 (c) and d)) and LFS discharge 92313 (e) and f)) at different time points. Here, s is the square-root of the normalised poloidal flux. Appearance of MHD and impurity accumulation is around 7.5 s and 8.5 s for discharges 92311 and 92313, respectively.*

Figure 3 shows the electron temperature and density for the HFS, central and LFS discharges. During the MHD activity that occurred in the HFS and LFS discharges the central electron density became peaked while the central electron temperature decreased and became flat in the centre, both effects enhance inward convection (5) which resulted in central impurity accumulation. Most of the impurity accumulation is due to W which for central plasma values its concentration ranges from $2.0 \cdot 10^{-5}$ at the beginning of the discharges to $1.5 \cdot 10^{-4}$ at the end, staying relatively constant at $1.5 - 2.0 \cdot 10^{-4}$ during the MHD activity. However, using the bolometer signals and assuming $Z_{eff} = 2.0$, taking Be as the only other impurity there is 10-30% missing radiation which belongs to a contribution of other mid-/high-Z impurities such as Ni and Mo. Regarding fusion

performance, figure 4 shows that only the discharge with a central resonance avoided impurity accumulation and maintained steady values for β_N, neutron production rate and electron temperature.
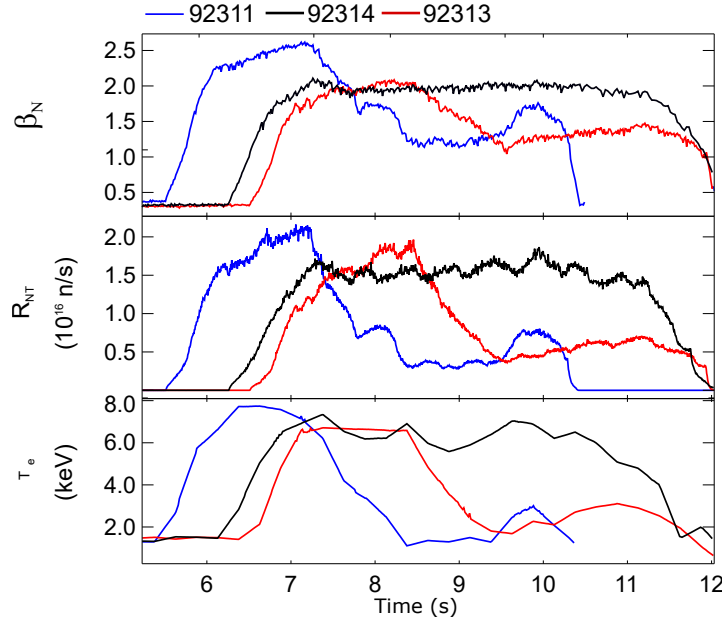
Figure 4: *Measured values for β_N, neutron production rate and electron temperature for discharges 92311 (HFS), 92314 (central) and 92313 (LFS).*
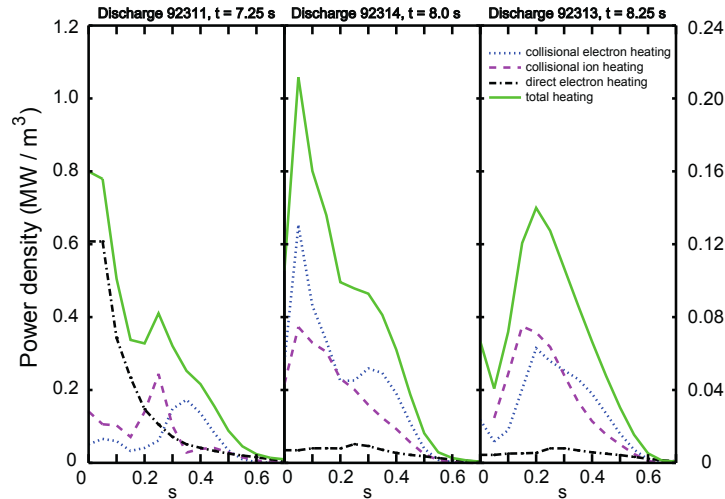
Figure 5: *Power density profiles for collisional ion heating, collisional electron heating, direct electron heating and total plasma heating due to ICRF waves as given by PION for discharges 92311, 92314 and 92313 with a HFS, central and LFS ICRF resonance, respectively. The profiles are shown after 1.75 s from the start of the main heating. The right y-axis has been normalised to the average ICRF input power of 5MW.*

The modelled heating profiles (figure 5) show differences as the resonance changes

from the HFS to the LFS. The evaluation of the heating profile provides valuable information regarding where the wave energy is being deposited and how strong fast ion pressure can be expected. Typically, central power deposition is preferable (s < 0.3) in order to obtain peaked plasma temperature profiles. PION takes into account orbit width effects which tend to broaden the orbits of the fastest ions and, therefore, collisional electron heating profile broadens with respect to bulk ion heating. Notice that changes in the toroidal magnetic field affect the orbit width as it is proportional to the Larmor radius, however it is limited to variations of $\pm 10\%$ for these set of discharges. Figure 5 shows that ion heating is marginally central for the HFS discharge as bulk ion heating peaks at s = 0.25 and collisional electron heating at s = 0.35, for the central discharge the power deposition peaks at the centre around s = 0.1 and for the LFS around s = 0.2. PION predicts strong central direct electron damping for HFS resonance discharge as T_e peaks at the centre (equation 1) and there are no other competing damping mechanisms. It becomes almost negligible as the resonance is placed towards the LFS, increasing from the edge until the competing ion damping mechanisms become dominant. In fact, the highest electron temperature was obtained in the HFS discharge until the appearance of MHD and impurity accumulation (figure 4). The power density of bulk ion heating and collisional electron heating are higher for central and LFS discharges. Collisional electron heating is the dominant heating mechanism in the central discharge which is beneficial to avoid central impurity accumulation as higher fast ion pressure and more peaked plasma temperature profiles are expected. The LFS discharge shows a similar bulk ion heating and collisional electron heating with the total heating power peak located off-axis around s = 0.2 while in the other two cases the total heating power peak is located in the centre. Regarding the ICRF power partition, it varies with the resonance position, however, other factors such as different temperatures and densities also play a role. The volume integrated average heating fractions as computed by PION are shown in table 3 for each discharge.

Table 3: ICRF volume integrated power fraction for fundamental H, 2nd harmonic D and direct electron damping as calculated by PION.

	HFS (%)	Central (%)	LFS (%)
Fundamental H	50	60	50
2nd harmonic D	15	30	40
Direct electron damping	35	10	10

The heating profiles predicted by PION have a direct impact on the calculated fast ion effective temperature. Not only on the average energy of the fast ion population but also on the position where the effective temperature is maximum which is important in order to compute the temperature gradients associated with the impurity screening (5). Figure 6 shows the effective temperature of fast minority for the HFS, central and LFS discharges. Also shown is the effective temperature for D for the central case, which is
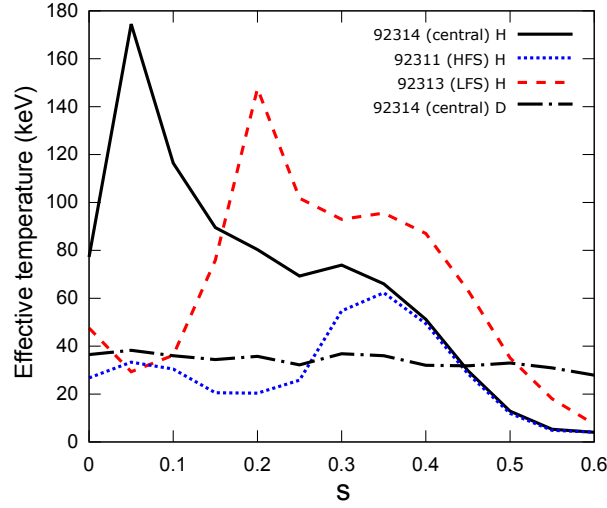
Figure 6: *Effective temperature of hydrogen minority ions for discharges 92311 (dotted), 92313 (dashed) and 92314 (solid). The dotted-dashed line is the D effective temperature for the central discharge.*

virtually the same in all discharges. The effective temperature for D has no gradient as predicted by PION and, therefore, only temperature screening associated to H minority ions is calculated. The effective temperature has been computed using $T_{\mathrm{f}} = \frac{2E_{\mathrm{f}}}{3n_{\mathrm{f}}}$ where n_{f} and E_{f} refer to the fast H minority density and energy density, respectively. Notice that the effective temperature broadens due to orbit width effects. We have evaluated the temperature screening by fast minority ions in comparison to the relative temperature screening associated to thermal D as $\Gamma_{\mathrm{f,H}}/\Gamma_{\mathrm{th,D}} = n_{\mathrm{f,H}} T_{\mathrm{th,D}}^{1/2} L_{\mathrm{th,D}}/(n_{\mathrm{th,D}} T_{\mathrm{f,H}}^{1/2} L_{\mathrm{f,H}})$, where $L_{th,D}$ and $L_{f,H}$ are the inverse of the logarithmic temperature gradient for thermal D and fast H. The gradient has been calculated over the s values shown in table 4, such as L_i uses $\mathrm{s}_{i+1} - \mathrm{s}_i$. The thermal and fast densities of H and D are shown in figure 7. The results of our analysis are shown in table 4. These results show that under these

Table 4: Computed temperature screening factor of H minority normalised to temperature screening factor provided by thermal D ($\Gamma_{\mathrm{f,H}}/\Gamma_{\mathrm{th,D}}$) for discharges 92311 (HFS), 92314 (central) and 92313 (LFS).

s	HFS (%)	Central (%)	LFS (%)
0.05	0.8	2.0	1.3
0.10	0.2	1.4	-1.2
0.15	2.0	1.0	-2.7
0.20	0.8	1.3	2.6
0.25	-4.0	0.0	-0.1

conditions impurity screening from fast minority ions is of the order of few percent with respect to that from thermal D. The central discharge shows the highest values
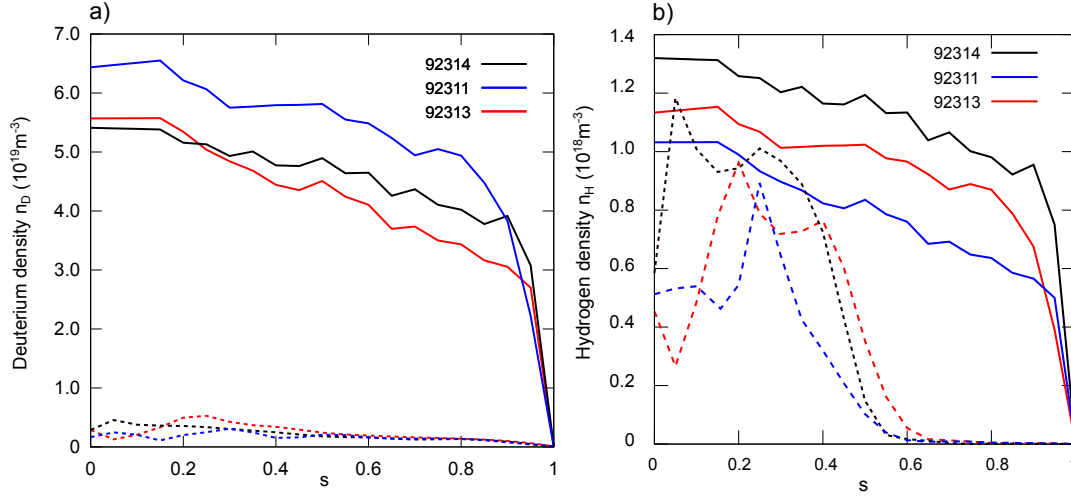
Figure 7: *Thermal (solid) and fast ion densities (dashed) for a) deuterium and b) hydrogen for discharges 92311 (blue), 92313 (red) and 92314 (black).*

for temperature screening in the centre. The HFS discharge has the lowest values of temperature screening except at s = 0.15 and a negative value at s = 0.25 as a result of a positive temperature gradient which enhances inward flux. In a similar way the LFS discharge has negative values at s = 0.10 and s = 0.15. These modelling results show that central ICRF heating is beneficial to avoid impurity accumulation as in other studies where it has been studied in detail [17, 18, 20]. However, it is difficult to draw firm conclusions regarding the relevance of fast minority ions among other mechanisms in these conditions as the experimental data show MHD activity and radiation peaking at the same time. For the rest of the hybrid discharges, central ICRF resonance was used.

6. Effect of hydrogen concentration on plasma performance

One of the goals was to assess the impact of the H concentration on the ICRF heating and optimisation of fusion performance. It is known that the H minority concentration plays a key role in the ICRF power partitioning (section 2.1) between H and majority D and beam-injected D ions which has an impact in the bulk ion heating and the fusion yield enhancement [11]. A set of discharges with different H concentration was implemented (figure 8). In all cases, central heating was performed in order to avoid MHD activity and impurity accumulation as seen in the previous section. The same plasma composition and plasma parameters were preserved in these discharges only changing the H concentration, see table 5 [26]. Here, we quote the H concentration $n_H/(n_H + n_D)$ as deduced from the ratio of the D_α and H_α light collected along lines of sight through the plasma. Penning gauge spectroscopy in the divertor gave somewhat higher $n_H/(n_H + n_D)$ of 3-4%. The radial profiles for the plasma temperature and density are very similar as shown in figure 9 for three different times, between the three
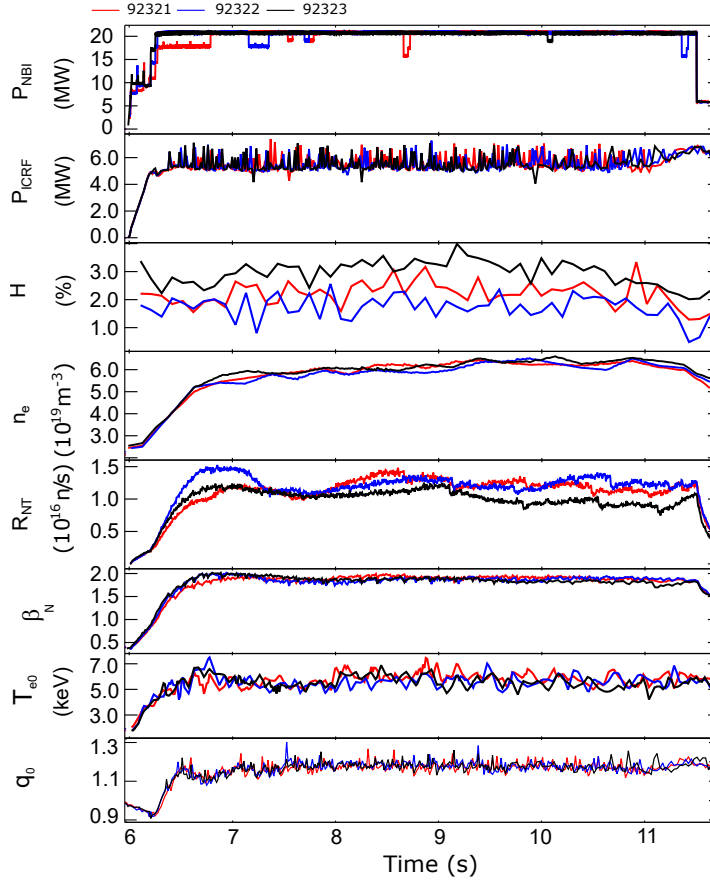
Figure 8: *Overview of three hybrid discharges with three different H concentrations. Different neutron rates are obtained for similar plasma parameters and power input as a consequence of slight variations in the H concentration. The H concentration data (dashed) has been smoothed (solid) for this plot.*

discharges.

According to our modelling, however, the experimental results are more consistent with the values deduced from the D_α and H_α light (figure 10). The main results in the experimental observations (figure 8) are the differences in the fusion yield for the three discharges. In the early stage of the heating phase up to t = 8 s discharge with the lowest H puff shows a faster rise in the neutron yield. A lower H concentration leads to a larger D damping of the wave energy (figure 11), accelerating them to higher energies with respect to the other discharges (figure 12). As the plasma density grows, the difference in the neutron rate is reduced. From t = 8 s onwards the fusion yield of the discharge with the lowest H concentration is in average ∼20% higher than in the discharge with the highest H concentration, which we interpret as being due to a stronger ICRF-accelerated fast deuterium tail.

The experimental results are in line with our modelling results. Figure 10 shows the simulated neutron rates for the three discharges which are consistent with the measured neutron rates [25]. The difference between the discharge with the lowest
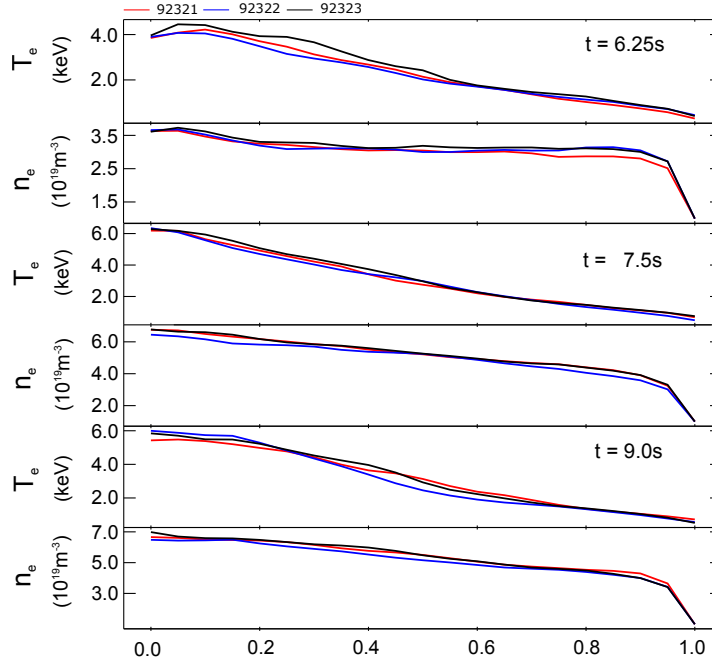
Figure 9: *Radial profiles for plasma temperature and density. The profiles are shown at three different times, during the ramp up $t = 6.25s$ and during the main heating phase, $t = 7.5$ and 9.0.*

Table 5: The range of H concentration for discharges in the H concentration scan.

	92321	92322	92323
$n_H/(n_H + n_D)$ (%)	1.5-3.0	1.0-2.0	2.5-4.0

H concentration and the discharge with the highest concentration is about 0-25% which is in good agreement with the experimental results. The difference vary as the H concentration is not constant throughout the discharge, the H(%) showed in figure 8 has been smoothed for a better visualisation. The ICRF wave was tuned for a central $\omega = \omega_{cH} = 2\omega_{cD}$ resonance for the three discharges. The variation of H concentration has a direct impact on the power partition between the H and D ions, this is shown in figure 11 at t = 10.0 s during the main heating phase. In first order, the ratio of H to D damping scales roughly as $n_H/(n_H+n_D)$, as expected. A comparison with the numerical result and the analytical approximation (equation 2) for the local power partition at the resonance is given in table 6. Both, numerical and analytical, follow the same trend, higher absorption from 2nd D harmonic resonance for lower H concentrations. PION follows the changes in the H concentration throughout the discharge and although the H concentration for these discharges is low, notice that small differences in the H concentration play a relevant role in this scenario as they have an impact in the way plasma damps the ICRF wave energy and consequently in the plasma performance. This is clearly evident in figure 12 where a lower H concentration leads to a stronger highly energetic D tail, further enhancing fusion performance as the second harmonic D
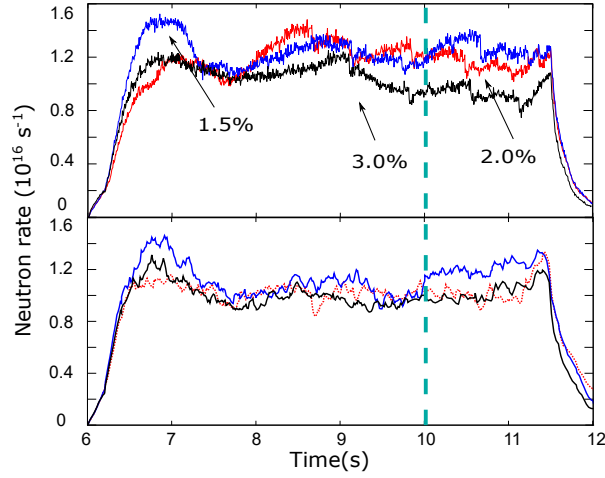
Figure 10: *Comparison of experimental neutron emission rate (top) for discharges 92321, 92322 and 92323 with a H concentration of about 2%, 1.5% and 3%, respectively. Modelled neutron emission rate of the H scan discharges (bottom). The vertical dashed line marks the time point at which the ICRF heating profiles are shown.*

Table 6: Local power fractions between H and D at the resonance position as computed by PION and as the analytical approximation equation 2 with $c_{21} = 0.2$ for t = 10.0s.

	92321	92322	92323
PION p_2/p_1	1.43	2.68	0.63
Eq. 2 p_2/p_1	1.94	2.26	0.64

damping has an advantageous effect on the fusion yield. Notice that H distribution is more energetic in the discharge with higher H concentration, in fact it stays dominant in front of the D distribution until around the E = 1.1MeV. The D velocity distribution function shows the same trend in the PION modelling and in the measurements with the neutron time-of-flight spectrometer TOFOR [40–42]. However, PION predicts a stronger D tail as compared to TOFOR for the discharge with the highest H concentration. For the comparison we have volume integrated the PION distributions inside s = 0.35 where most of the TOFOR signals come from and we have averaged the distributions over the given TOFOR time window, the distributions are normalised so as to have 1 at E = 150keV. Notice that the cross section for DD fusion reactions peak at the MeV range and, therefore, strengthening the ICRF-accelerated deuterium tail enhances the fusion neutron rate for this particular case. As it is shown in figure 11, after the deuterium beams have been injected, 2nd D harmonic resonance becomes the main damping mechanism at the plasma centre for the two lowest H concentration discharges once the plasma core gets hotter, while fundamental H resonance dominates (figure 13) for low plasma densities and temperatures that take place during the ramp up (figure 8 and figure 9). Fundamental heating becomes more relevant at low temperatures as compared to 2nd harmonic heating since the RF diffusion is low at low temperatures for
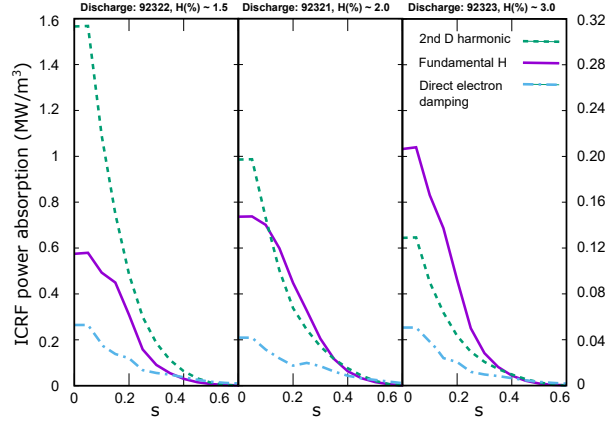
Figure 11: *ICRF power absorption profile for fundamental H (solid), 2nd D harmonic resonance (dashed) and direct electron damping (dashed-dotted) during the main heating phase at t = 10.0 s. The ICRF power absorption has been normalised to the average input ICRF power of 5MW (right y-axis).*

harmonic heating while it is higher for fundamental heating. This fact together with the low plasma density which decreases the critical energy and the collisionality favours the creation of energetic H ions which mainly collide with electrons. Other mechanisms can also influence the power absorption such as the q-profile, however there is a minor variation of q at the centre (figure 8) of around 15% from the ramp up to the main heating phase, for which PION does not predict differences in the power absorption fraction. Small to no differences are predicted by PION with regards to direct electron damping, therefore, varying the H concentration in a small range has no impact in the total fraction of energy absorbed by ions and electrons but only in the competing damping mechanisms by ion species.

Figure 13 shows the time evolution of fundamental H absorption, 2nd D harmonic absorption and direct electron damping for discharges with the lowest and highest H concentration. Similar behaviour is observed in the way damping mechanisms evolve, i.e. fundamental H damping dominates during the ramp up while it decays once the D beams are injected as they produce a rapid increase of the 2nd D harmonic damping strength. As the H concentration decreased from 3% to 1.5%, D damping increased from 35% to 50% and H damping decreased from 50% to 35% in average, while direct electron damping stayed roughly the same, i.e. 15% of the total ICRF power. Notice the decrease in H absorption for both cases around t = 11s as a consequence of the decrease in H concentration (figure 8) followed by an increase around t = 11.5s as the NBI beams are stopped around t = 11.3s.

7. High-performance hybrid discharge

From the point of view of fusion neutron rate, there was the aim to improve the previous record of $2.3 \cdot 10^{16}$ n/s from hybrid discharge 86614. The neutron rate record was achieved
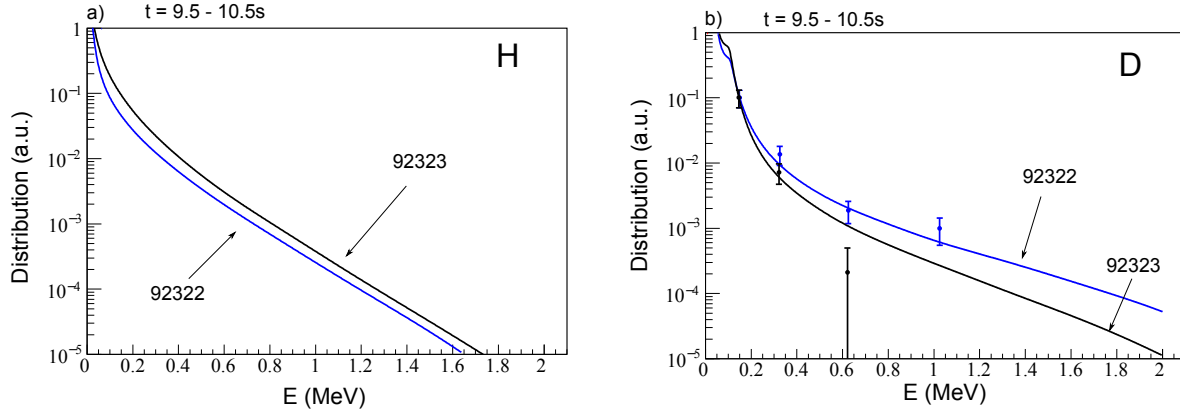
Figure 12: *Energy distribution functions of a) hydrogen and b) deuterium in logarithmic scale for discharges 92322 (blue) and 92323 (black) with a H concentration of about 1.5% and 3%, respectively. a) PION velocity distribution for H and b) PION velocity distribution for D and as deduced from measurements with the neutron time-of-flight spectrometer TOFOR (dots).*
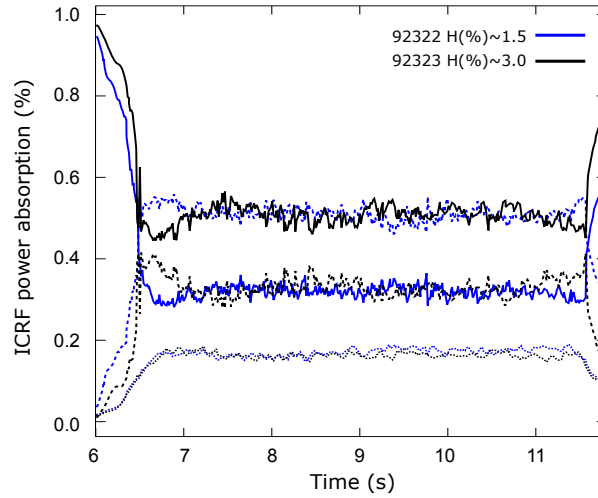
Figure 13: *Damping fractions of the total ICRF power with fundamental hydrogen absorption (solid), 2nd deuterium harmonic absorption (dashed) and direct electron damping (dotted) for discharges 92322 (blue) and 92323 (black). The D NBI power is stopped down at around $t = 11.3s$, resulting in the decrease in D damping fraction. A more detailed explanation for the differences in the ramp up and end of the discharge is given in this section.*

in several discharges and here, we study the combined effect of ICRF and NBI heating in one of the best shots with $B_T = 2.8$ T and $I_p = 2.2$ MA, discharge 92398. Similarly to other hybrid discharges, 5 MW of ICRF power was tuned to a central fundamental H and second D harmonic resonance ($\omega = \omega_H = 2\omega_D$) using a frequency of 42.5 MHz as in previous sections. Together with deuterium NBI power of 26 MW, the total external heating power was 31 MW. An overview of the high performing hybrid discharge 92398

is presented in figure 14. The neutron rate and normalised plasma beta increased to their steady-state values of $2.7 \cdot 10^{16}$ s^{-1} and 2.7, respectively, when stationary high-performance plasma was obtained.
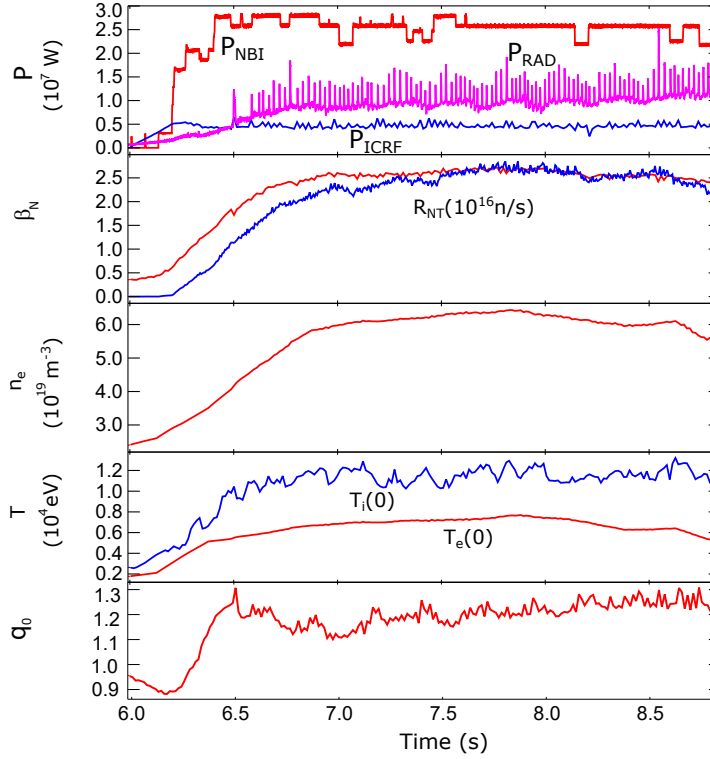

Figure 14: *Overview of the high performing hybrid dicharge 92398. A factor $R = T_i/T_e$ has been applied to the T_i as measured by the X-ray crystal spectroscopy (XCS) diagnostic.*

The experimental ion temperature T_i has been computed using the T_i/T_e ratio as deduced from the X-ray crystal spectroscopy data. This data suggests that the T_i/T_e ratio is around 1.25-1.6. The H concentration $n_H/(n_H + n_D)$ deduced from the ratio of the D$_\alpha$ and H$_\alpha$ light collected along lines of sight through the plasma is $\sim$2% and has been used to model this discharge. The calculated and experimental neutron yield are in good agreement as shown in figure 15. However, several uncertainties associated with the experimental measurements have been taken into account to assess their impact on the neutron yield (shaded area in figure 15). In particular, the upper limit of the shaded area represents the neutron rate value for a simulation assuming the maximum measured ratio by the XCS diagnostic of $Ti/Te = 1.6$ while the lower limit is for $T_i/T_e = 1.25$. The impurity content has been varied for $\pm 2\%$ around the measured impurity densities, the variation caused in the neutron rate falls inside the estimated error area. Radial profiles during the ramp up and main heating phase are provided in figure 16. One of the main goals was to evaluate the impact of ICRF enhancement in the fusion yield. In order to do so, the neutron rate has been modelled in two different ways, one which takes into account the full external power and a second one which only models the NBI heating
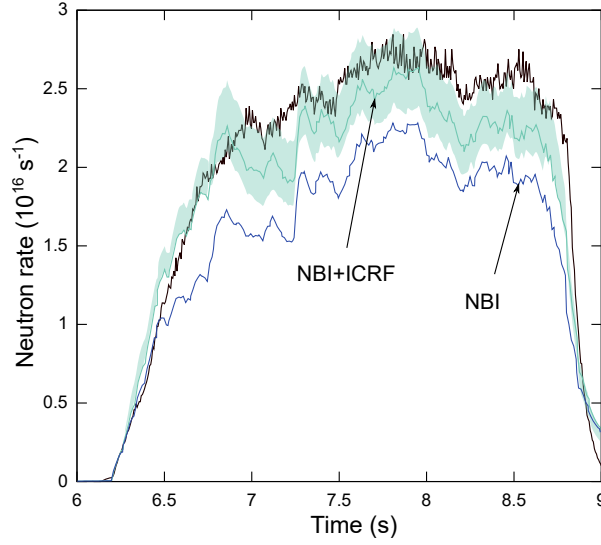
Figure 15: *Neutron production rate of discharge 92398. The solid black line is the experimentally measured neutron rate, the other two lines labelled as NBI+ICRF and NBI refer to the PION modelling for the total input power heating and only NBI, respectively. The shaded area shows the assumed error in the modelling due to uncertainties in the input ion temperature and impurity concentrations.*
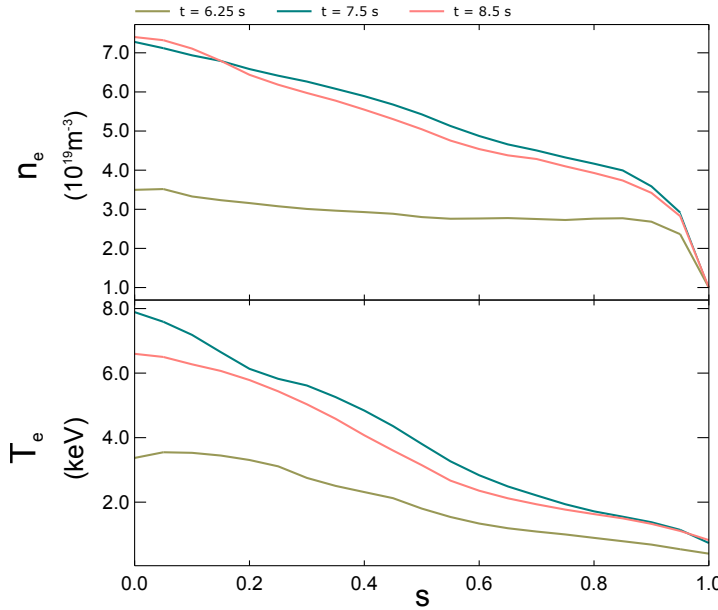
Figure 16: *Plasma density and temperature profiles for discharge 92398, at $t = 6.25s$ during the ramp up and at $t = 7.5$ and $8.5s$ during the main heating phase.*

(figure 15). The NBI only case has been modelled with PION with zero antenna power and using the beam source terms from PENCIL. The ICRF enhancement is calculated from the difference between the associated neutron yields for both heating mechanisms as $\mathrm{RF}(\%) = \frac{\mathrm{R_{NT}(NBI+ICRF) - R_{NT}(NBI)}}{\mathrm{R_{NT}(NBI+ICRF)}}$. Figure 17 shows good agreement between the ICRF

enhancement as estimated from a spectroscopic analysis of data collected by the neutron time-of-flight spectrometer TOFOR and as predicted by the PION code. Detailed explanation on the TOFOR neutron spectrum from NBI heating is provided in [43]. The enhancement varies throughout the discharge, starting at a maximum value of around 35% during the ramp-up phase and reaching a steady value of 15% during the main heating phase. This variation is the result of an increasing plasma density and temperature, as neutron emission from D beams and thermal reactions increase and, therefore, the ICRF enhancement is reduced until a steady value. However, notice that this enhancement does not extrapolate to DT scenario as will be shown in section 8.2 since the fusion cross sections σ_{DT} and σ_{DD} are different.
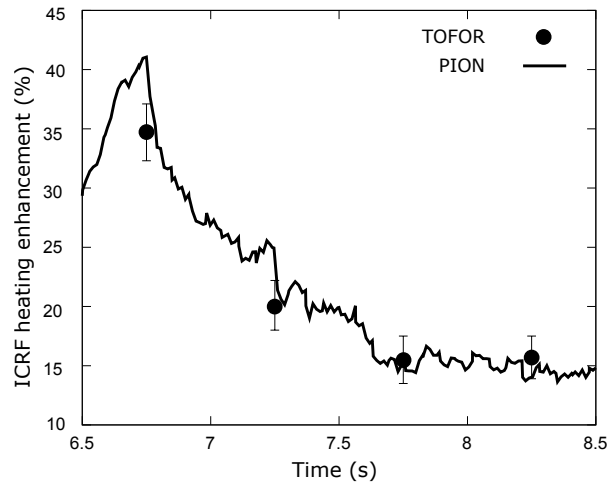

Figure 17: *ICRF enhancement of neutron yield for discharge 92398. Comparison of PION (solid line) and experimental results based on TOFOR (black dots) measurements.*

In order to maximise the ICRF fusion enhancement in this scenario, it is crucial that D ions absorb most of the ICRF wave power and the presence of a high bulk ion heating as mentioned in section 2.2. The damping mechanisms competing in this discharge are the same as those described in section 6 and the physics are similar. During the ramp-up, fundamental H absorbs almost all the wave power while 2$^{\text{nd}}$ D harmonic damping becomes dominant during the main heating phase (figure 18 a)).The absorption profile (figure 19) shows a strong absorption of fundamental H for low plasma temperatures while it becomes lower during the main heating phase where D absorption becomes dominant as seen in section 6. Bulk ion heating is dominant throughout the whole discharge except for the low temperatures and densities that characterise the ramp-up phase (figure 18 b)), where fundamental H strongly dominates generating a fast ion population that slows-down mainly through ion-electron collisions. PION predicts an average fast ion energy of 500 keV for minority H at t = 6.25 s where fundamental H absorption peaks and 160 and 65 keV for H and D, respectively, during the main heating phase. The computed critical energies are 115 and 230 keV for H and D, respectively, during the main heating phase. Our modelling results show higher bulk ion heating

than electron heating during the main heating phase from t = 6.5s onwards. While full heat transport analysis is beyond the scope of the present study, this appears consistent with the measured higher T_i than T_e.
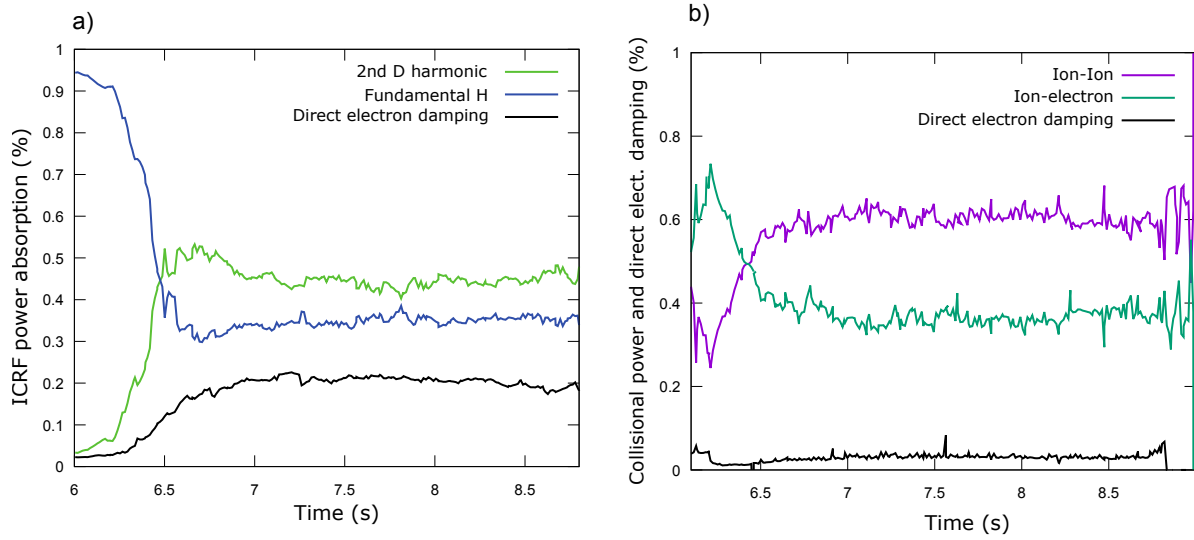
Figure 18: *a) Normalised ICRF power absorption mechanisms to the input ICRF power, fundamental H, 2nd D harmonic and direct electron damping for discharge 92398. b) Normalised direct electron damping and collisional power transferred to ions and electrons from ion-ion collisions and ion-electron collisions to the total input power ICRF+NBI.*
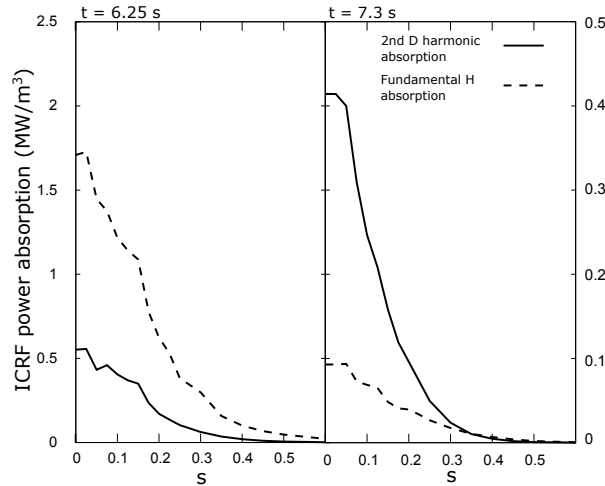
Figure 19: *Absorption profile for fundamental H absorption (dashed) and 2nd D harmonic absorption (solid) at t = 6.25 s and t = 7.3 s. The right y-axis has been normalised to the average ICRF input power of 5MW.*

8. Predictions for DT

The prediction for a DT discharge is the last step in the analysis of the high-performance hybrid discharges, where the maximum power output and the best strategy to follow is studied. This section tackles two different topics: the DT fusion yield and the maximization of bulk ion heating from the prediction of a high-performance hybrid discharge.

8.1. DT fusion yield prediction

In order to model a 50%:50% DT plasma from the high-performance discharge 92398, the plasma composition has been modified by changing half of the bulk D by T and half of the D beams by T. The stand-alone simulations for PION take a single time point of the original discharge, in this case 92398, and evolve until a steady state solution is found. Quasi-neutrality is maintained in all cases since the electron density is computed as $n_e = \sum_i Z_i n_i$ in both codes PION and PENCIL. The NBI penetration is calculated by the PENCIL code under the presence of T for both beam species, D and T. The collisionality is computed in PION for all resonant species with the background plasma defined as 50%:50% DT. The magnetic equilibrium is assumed to be as in discharge 92398 and, therefore, does not take into account the change in the Grad-Shafranov shift at the magnetic axis. An estimation of the shift at the magnetic axis due to the presence of T in the plasma with regards to the pure D scenario has been carried out using the Grad-Shafranov shift equation as given in [44]. The plasma energy increases around 30-35% from pure D to DT plasma, assuming the internal inductance to be constant, the Grad-Shafranov shift at the magnetic axis increases approximately in 2-4cm. This is in line with the DT prediction simulations performed in [19] where an increase of 3cm was found. Such a small change will have a very small impact in the simulations performed in the present section and section 8.2. However, in case that larger shifts occur, the resonance position would be placed further off-axis at the HFS. This could be solved by slightly tuning the toroidal field as to match the central resonance. In this new scenario, the ICRF scheme changes as T becomes resonant together with H and D. However, as discussed in section (2.1) and showed in equation (3) the damping strength of 3rd T harmonic is negligible as compared to that of H or D. In fact, as D and T beams are injected, the 2nd D harmonic becomes the dominant damping mechanism as expected. Nevertheless, while previous sections hinged around the idea that channeling most of the power to D was beneficial for the fusion performance, it does not necessarily apply in the DT scenario (section 2.2). The reason is that fusion DD and DT cross sections peak at different energy regions, while DD cross section peaks around the MeV range, D→T cross section peaks around 120 keV and decreases rapidly beyond this energy. Therefore, one needs to be careful in the way energy is channeled to D as a strong high energy tail in the distribution function has the potential to decrease the number of fusion reactions. As beams are close to the optimal energy for DT fusion reactions to occur, most of the fusion reactions are due to beam-thermal ion interactions and thus,

a lower ICRF enhancement is expected as compared to the DD scenario which is about 5% in this case. PION predicts an equivalent DT fusion power of about 7 MW and 12.9kW of DD fusion power.

8.2. Combined NBI + ICRF heating in JET DT plasmas

Bulk ion heating and ICRF fusion enhancement are relevant quantities in order to evaluate DT plasmas. An increased neutron rate should be obtained by maximising both. The following discussion shows the results obtained with coupled PENCIL and PION and studies the dependence of bulk ion heating and ICRF fusion enhancement under a scan on key plasma parameters. A 50%-50% DT fuel ion mixture is considered under a scan in plasma temperature and density of the hybrid discharge 86614 ($n_e = 6.2 \cdot 10^{19}$ m^{-3}, $T_e = 9$ keV). The NBI source rate is shown in figure 20 for the different plasma densities considered at $T_e = 9$keV. The prediction is carried out in the same way as it has been performed in the previous section. Ion and electron temperatures are assumed to be equal. The toroidal magnetic field is set to $B_T = 3.25$ T and the plasma current to $I_p = 2.7$ MA. A total heating power of 40 MW has been simulated consisting of 34 MW of NBI power (17 MW of D beams and 17 MW of T beams) and 6 MW of ICRF power, in several simulations the ICRF power has been set to zero for comparison purposes. Regarding the ICRF scheme a comparison between H and ^{3}He as minority species has been performed while the simulated antenna frequency has been set for central heating for all the cases under consideration. The resonant ion
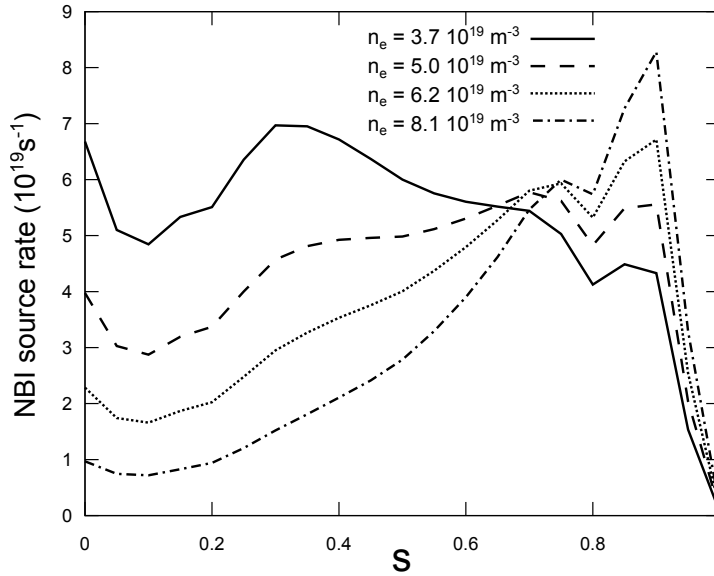

Figure 20: *NBI source rate for $T_e = 9$keV for different plasma densities.*

absorption strength for both minority scenarios ranges from 63% to 87% and 73% to 90% for H and ^{3}He minority scenarios, respectively (figure 21). Minority concentrations for H and ^{3}He are maintained constant at 5% over D and T densities, $\frac{n_H}{n_D+n_T}$ and $\frac{n_{3He}}{n_D+n_T}$, respectively. PION predicts a dependency of the power absorption on both,

the plasma density and the plasma temperature. For lower plasma temperatures and densities the power absorption is higher while it decreases for higher values of plasma temperature and density where direct electron damping is stronger as it is $\propto T_e n_e$. However, ion absorption is dominant over direct electron damping for the whole range under consideration.
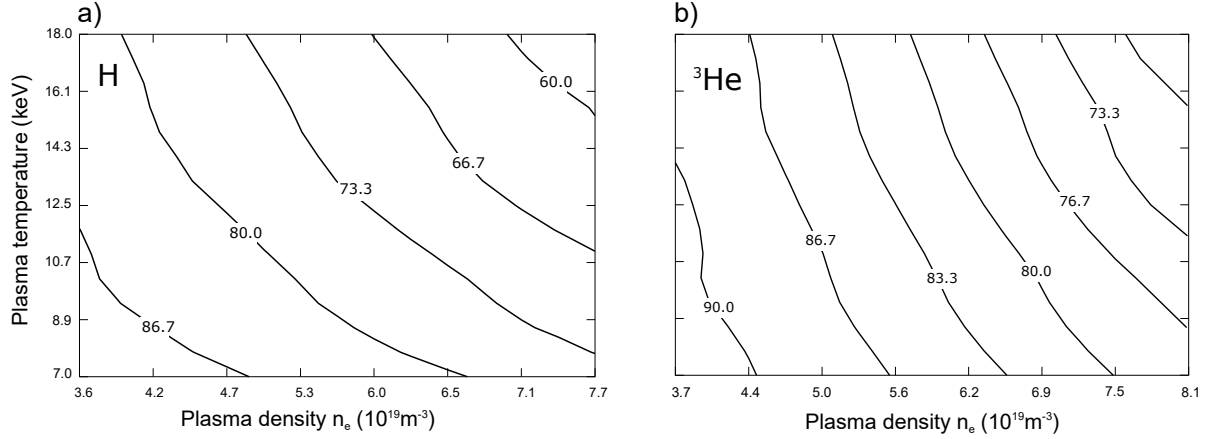
Figure 21: *Contour lines of normalised power absorption of resonant ions to total RF input power (6MW) in % for a minority concentration of 5%, a) H minority and b) ^{3}He minority.*

Bulk ion heating is shown in figure 22. Although D and T beams are used for both minority scenarios, i.e. H and ^{3}He, only resonant species are shown, therefore, only T beams (17 MW and $\sim$ 95 keV) are shown in the ^{3}He minority case and only D beams (17 MW and $\sim$105 keV) in the H minority case as they are resonant through the 2nd harmonic resonance. Tritium beams are resonant in the H minority scenario but the 3rd T harmonic resonance absorption strength is negligible in front of the 2nd D harmonic and H fundamental absorption strength as predicted by PION under the conditions of this scenario.

For all the range under consideration of the pure NBI simulated scenario, between 65-90% of the D NBI power and 82-100% of the T NBI power is transferred to ions, this difference lies in the higher energy of D beams and a higher critical energy of T beams as $E_{crit} \propto A$ (see (4)). The simulations with NBI+ICRF show a different trend and the differences between both minority scenarios grow. As the critical energy increases with T_e the collision power from resonant ions to thermal ions depend mainly on the plasma temperature. However, as compared to the simulated pure NBI scenario, the NBI+RF scenario shows an increase of bulk ion heating with plasma density. The reason why this occurs is that the average energy of fast ions tends to decrease and the direct electron damping becomes relatively stronger for increasing plasma densities. Both effects tend to increase the proportion of fast ion energy transferred to ions by lowering the average fast ion energy (see figure 1). Regarding the differences between both minority scenarios, the ^{3}He minority scenario shows a 15-20% higher bulk ion heating, mainly due to a
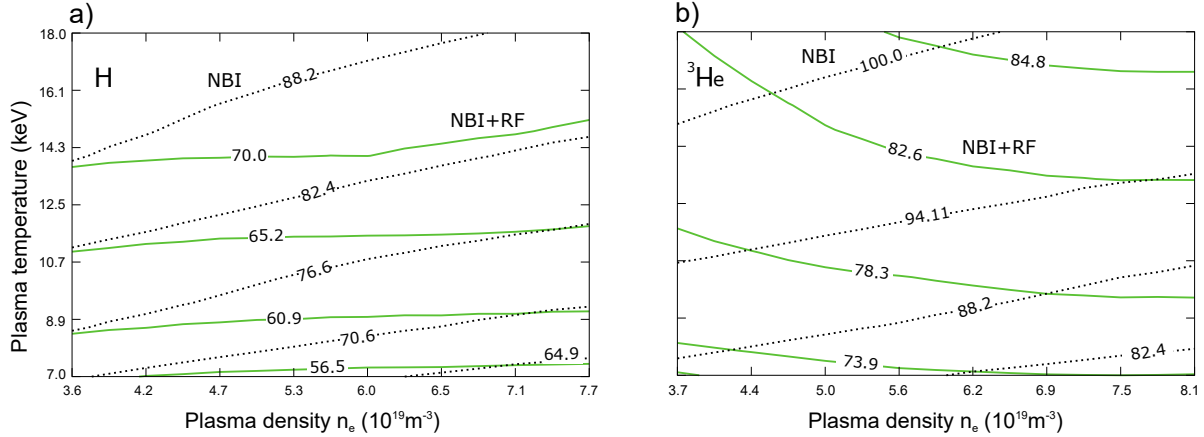
Figure 22: *Contour lines of normalised collisional power from resonant ions to thermal ions for NBI and NBI+RF to total RF input power (6MW) and resonant beam power (17MW) in % for a minority concentration of 5%, a) H minority and b) ^{3}He minority.*

higher critical energy of ^{3}He as compared to H and the lower direct electron damping in the ^{3}He minority scenario. A scan in the minority concentration at $T_e = 9$ keV and $n_e = 6 \cdot 10^{19}$ m^{-3} is presented in table 7. Bulk ion heating increases with the minority concentration for both cases as the average fast ion energy decreases. For higher minority concentrations the absorption tends to become weaker for fundamental heating as the polarization of the wave changes due to high minority concentration in the plasma.

Table 7: Bulk ion heating in MW for a scan in the minority concentration.

Minority	1%	3%	5%	7%
H	13.5	13.7	13.9	14.1
^{3}He	16.1	17.0	17.7	18.0

The motivation for modelling the ICRF fusion enhancement of the DT scenario (figure 23) comes from the fact that, in principle, ICRF heating can accelerate deuterons and tritons beyond the optimal DT fusion reaction energy ($\sim$120 keV for fast D and $\sim$160 keV for fast T), which could result in a lower fusion yield. However, figure 23 shows that this is not the case for the parameter range under consideration as the ICRF enhancement is positive in both minority scenarios. The ^{3}He scenario shows a lower ICRF enhancement of the DT fusion reaction rate as the T damping strength is roughly 10% of the total D damping strength for the H minority scenario. Nevertheless, the ICRF fusion enhancement behaves in a similar way for both minority scenarios, it is lowest at regions where thermal fusion reactivity increases, i.e. regions of higher plasma density and temperature. The ICRF enhancement ranges from 2-9% for H minority scenario and 0.5-2% for ^{3}He minority scenario.
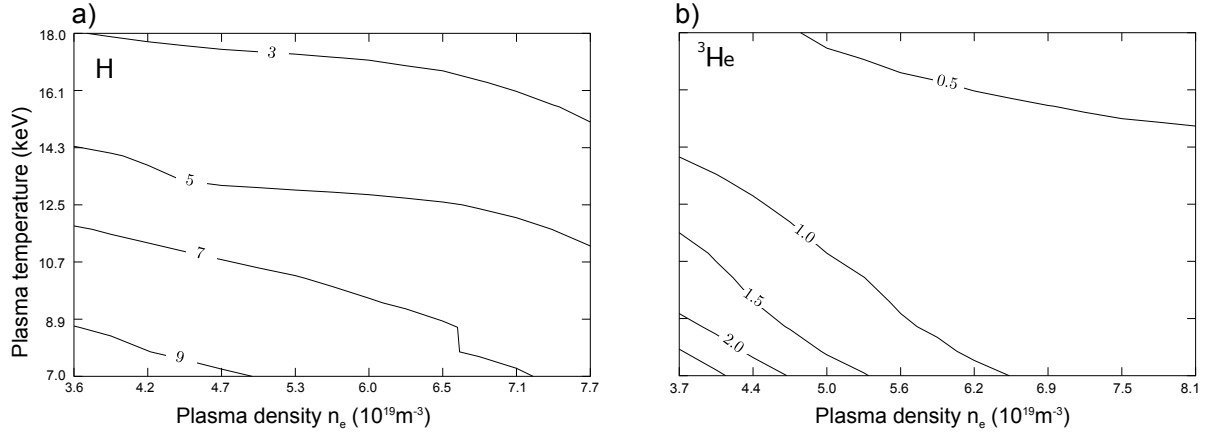
Figure 23: *Contour lines of the ICRF fusion enhancement of D+T reaction rate in %
of the total $\frac{R_{NT}(NBI+RF)-R_{NT}(NBI)}{R_{NT}(NBI+RF)}$, a) H minority and b) ^3He minority.*

9. Conclusions

A number of key topics related to the use of ICRF waves in hybrid plasmas have
been modelled and analysed in this paper, such as the impact of ICRF resonance
location on the impurity accumulation, the importance of H minority concentration
on the ICRF performance and the ICRF properties and neutron yield enhancement of a
high-performance hybrid discharge in addition to its DT prediction. It has been shown
that heating with ICRF waves centrally has beneficial effects in order to avoid impurity
accumulation while heating further away from the centre can cause MHD activity and
impurity accumulation under these conditions ($|R_{res} - R_0| > 15$cm). In this scenario,
channeling the maximum ICRF power to D has an advantageous effect in the fusion
yield, ranging from 0 to 25% by lowering the H concentration which tends to make
2nd D harmonic resonance more dominant. Therefore, the modelling of this scenario
supports central ICRF heating and low concentration of the minority in order to extend
the duration of high plasma performance, i.e. high neutron rate and avoidance of central
impurity accumulation. Regarding the ICRF enhancement in the neutron rate, a steady
15% enhancement was achieved in a high-performance discharge during the main heating
phase and 30% during the ramp-up. However, the enhancement in the DT prediction
is diminished, mainly due to the different fusion cross sections of DD and DT fusion
reactions. The modelling of the DT prediction shows an improved bulk ion heating
of the order of 15-20% for the ^{3}He minority scheme as compared to the H minority
scheme, while ICRF fusion enhancement is predicted to be higher in the H scheme as
2nd D harmonic resonance shows a stronger absorption as compared to 2nd T harmonic
resonance in the ^{3}He minority scheme.

Acknowledgements

References

[1] C.K. Phillips *et al.*, Physics of Plasmas **2** (1995) 2427.
[2] J.R. Wilson *et al.*, Physical Review Letters **75** (1995) 842.
[3] L.-G. Eriksson *et al.*, Nuclear Fusion **39** (1999) 337.
[4] D.F.H. Start *et al.*, Physical Review Letters **80** (1998) 4681.
[5] D.F.H. Start *et al.*, Physical Review Letters **39** (1999) 321.
[6] M.-L. Mayoral *et al.*, Nuclear Fusion **46** (2006) 7 S550.
[7] E.F. Jaeger *et al.*, Physics of Plasmas **15** (2008) 072513.
[8] M.J. Mantsinen *et al.*, Plasma Phys. Control. Fusion **45** (2003) A445-A456.
[9] M.J. Mantsinen *et al.*, Phys. Rev. Lett. **88** (2002) 10 105002.
[10] Ye.O. Kazakov *et al.*, Nature Physics **13** (2017) 973.
[11] M.J. Mantsinen *et al.*, Plasma Phys. Control. Fusion **41** (1999) 843.
[12] G.A. Cottrell *et al.*, Nuclear Fusion **39** (1999) 389.
[13] F.G. Rimini *et al.*, Nuclear Fusion **39** (1999) 1591.
[14] R.W. Harvey *et al.*, Nuclear Fusion **26** (1986) 1 43.
[15] V.B. Krapchev *et al.*, Nuclear Fusion **25** (1985) 4 455.
[16] C. Angioni *et al.*, Nuclear Fusion **57** (2017) 056015.
[17] M. Goniche *et al.*, Plasma Phys. Control. Fusion **59** (2017) 055001.
[18] E. Lerche *et al.*, Nuclear Fusion **56** (2016) 3 036022.
[19] J. Garcia *et al.*, Plasma Physics and Controlled Fusion **59** (2017) 014023.
[20] T. Casper *et al.*, Nuclear Fusion, **54** 1 (2014) 013005.
[21] C. Gormezano *et al.*, Fusion Science and Technology, 53 (2008) 958.
[22] X. Litaudon *et al.*, Nuclear Fusion, **57** (2017) 102001.
[23] L.-G. Eriksson *et al.*, Nuclear Fusion **33** (1993) 1037.
[24] P.M. Stubberfield *et al.* Multiple Pencil Beam, JET-DPA(06)/87, 1987.
[25] M.J. Mantsinen *et al.*, European Journal of Physics **157** (2017) 03032.
[26] M.J. Mantsinen *et al.*, Europhysics Conference Abstracts vol. 41F (2017) O3.110.
[27] D. Gallart *et al.*, European Journal of Physics **157** (2017) 03015.
[28] D. Gallart *et al.*, Europhysics Conference Abstracts vol. 40A (2017) P2.003.
[29] M. Porkolab *et al.*, Plasma Phys. Control. Fusion **40** (1998) A35.
[30] F.J. Casson *et al.* Plasma Phys. Control. Fusion **57** (2015) 014031.
[31] C. Angioni and P. Helander Plasma Phys. Control. Fusion **56** (2014) 124001.
[32] M.Valisa *et al.* Nucl. Fusion **51** (2011) 033002.
[33] M.L. Reinke *et al.* Plasma Phys. Control. Fusion **54** (2012) 045004.
[34] M. Goniche *et al.* Europhysics Conference Abstracts vol. 38F (2014) 04.129.
[35] T.C. Hender *et al.* Nuclear Fusion **56** (2016) 066002.

[36] T.H. Stix, Plasma Physics **14** (1972) 367.

[37] L.-G. Eriksson *et al.* Physics of Plasmas **1** (1994) 308.

[38] L.-G. Eriksson *et al.* Physica Scripta **55** (1995) 70.

[39] T. Hellsten *et al.*, Physics of Plasmas **24** (2017) 022122.

[40] M. Gatu Johnson *et al.*, Nucl. Instrum. Methods A, 591 (2008) 417.

[41] C. Hellesen *et al.*, Nuclear Fusion **53** (2013) 113009.

[42] C. Hellesen *et al.*, Nuclear Fusion **58** (2018) 056021.

[43] C. Hellesen *et al.*, Plasma Phys. Control. Fusion **52**(8) (2010) 085013-10.

[44] J. Wesson, Oxford Science Publications, Clarendon Press, Oxford, 1997.